Journal of
Materials Chemistry A

ROYAL SOCIETY OF CHEMISTRY

Structure-Property Relationships Describing the Buried Interface Between
Silicon Oxide Overlayers and Electrocatalytic Platinum Thin Films

SCHOLARONE™
Manuscripts

Structure-Property Relationships Describing the Buried Interface Between

Silicon Oxide Overlayers and Electrocatalytic Platinum Thin Films

Marissa E.S. Beatty,[†] Han Chen,[†] Natalie Y. Labrador, Brice J. Lee, Daniel V. Esposito*

Columbia University in the City of New York

Department of Chemical Engineering

Columbia Electrochemical Energy Center,

Lenfest Center for Sustainable Energy

500 W. 120th St., New York, NY 10027

[†]both authors contributed equally

*Corresponding Author

email: de2300@columbia.edu

phone: 212-854-2648

Abstract

Encapsulation of an active electrocatalyst with a permeable overlayer is an attractive approach to simultaneously enhance its stability, activity, and selectivity. However, the structure-property relationships that govern the performance of encapsulated electrocatalysts are poorly understood, especially those describing the electrocatalytic behavior of the buried interface between the overlayer and active electrocatalyst. Using planar silicon oxide (SiO_x)-encapsulated platinum (Pt)/titanium (Ti) bilayer thin films as model electrodes, the present study investigates the physical and electrochemical properties of the $SiO_x|Pt$ buried interface. Through a combination of X-ray photoelectron spectroscopy and electroanalytical measurements, it is revealed that a platinum oxide (PtO_x) interlayer can exist between the SiO_x overlayer and Pt thin film. The thickness and properties of the PtO_x interlayer can be altered by modifying the i.) thickness of the SiO_x overlayer or ii.) the thickness of the Pt layer, which may expose the buried interface to oxophilic Ti. Importantly, $SiO_x|Pt$ electrodes based on ultrathin Pt/Ti bilayers possess thinner PtO_x interlayers while exhibiting reduced permeabilities for Cu^{2+} and H^+ and enhanced stability during cycling in 0.5 M H_2SO_4. These findings highlight the tunability of buried interfaces while providing new insights that are needed to guide the design of complex electrocatalysts that contain them.

I. Introduction

Electrocatalysts are essential components in fuel cell and electrolysis technologies, which are expected to play key roles in a sustainable energy future by enabling the efficient interconversion between renewable electricity and chemical fuels.[1–3] For most commercial electrolyzers and fuel cells, electrocatalysts take the form of metallic nanoparticles that are attached to conductive electrode supports while simultaneously remaining in contact with an ion-conducting electrolyte phase. Conventionally, these electrocatalysts are also exposed to a gaseous or liquid phase that contains the electroactive species of interest, creating so-called triple-phase sites. This "exposed" configuration is generally desirable because it allows for facile transport of reactants and products to and from the electrocatalytically active sites. However, it also presents challenges for electrocatalyst stability because electrochemical and/or physical processes can promote nanoparticle agglomeration and/or dissolution of the electrocatalyst.[4]

In recent years, alternative electrocatalyst designs have been explored in which the active electrocatalyst is entirely encapsulated by ultrathin oxide overlayers that are permeable to the electroactive species of interest.[5–10] Encapsulation is an attractive approach to improve both the stability and catalytic properties of the active electrocatalyst compared to its exposed form. From a stability standpoint, overlayers can serve as a nanoscale adhesive that mitigates particle migration and loss of electrochemically active surface area (ECSA).[7,8] Additionally, oxide overlayers can serve as selective barriers, or membranes, that can further promote electrocatalyst stability by blocking impurity species from poisoning the catalyst surface.[10,11] Due to this membrane functionality, encapsulated electrocatalysts can be referred to as membrane coated electrocatalysts (MCECs). By leveraging selective transport properties, the overlayers of MCECs can alter the selectivity of competing electrochemical reactions by altering the concentrations of reactants at the buried interface between the active catalyst and overlayer.[9,12,13]

Encapsulation of electrocatalysts by thin overlayers can also alter reaction energetics and pathways by mechanisms other than selective transport.[12] These non-transport mechanisms often rely on the fact that the buried interface between the metallic phase and overlayer represents a confined environment where reactive intermediates are interacting simultaneously with the metal and overlayer. When active sites are located in confined environments, the steric, chemical, and/or electronic properties of reactive intermediates can be expected to be significantly altered relative to the same species located at the interface between a conventional electrocatalyst and the bulk electrolyte phase.[14–16] These confinement effects, combined with selective transport properties of the overlayer, make MCECs a highly tunable electrocatalyst architecture that may be engineered to achieve better selectivity and activity than conventional electrocatalysts. However, the large number of control knobs in MCECs, combined with inherent difficulties of characterizing buried interfaces, makes it extremely difficult to uncover the structure-property relationships that govern the performance of MCECs.

In order to better understand reaction energetics at buried interfaces and distinguish between different reaction mechanisms occurring there, it is essential that more detailed knowledge about the physical, chemical, and electronic properties of the buried interface be developed. If structure-property relationships of the buried interface can be clearly established and linked to electrocatalytic behavior, they can serve as design rules for optimizing the performance of MCECs. Towards this end, the current paper explores model MCECs based on ultrathin (1-10 nm thick) silicon oxide (SiO_x) overlayers deposited on smooth Pt thin films (Figure 1a). The thickness of SiO_x overlayers is controlled with nanoscale precision using a low temperature photochemical deposition process,[11] and the planar nature of these samples make

them well-suited for characterizing the physical and electrochemical properties of the $SiO_x|Pt$ buried interface.

The current study expands on two recent publications by our group that investigated the electrocatalytic properties of $SiO_x|Pt$ electrodes based on two different Pt thin film substrates. In the first study,[11] it was shown that SiO_x overlayers deposited on ultrathin bilayers of 3 nm Pt on 2 nm titanium (Ti) can behave as membranes that support the diffusive flux of protons (H^+) and hydrogen (H_2) molecules while blocking transport of Cu^{2+}, a poison for the hydrogen evolution reaction (HER). More recently, we reported that $SiO_x|Pt$ electrodes based on 50 nm thick Pt substrates exhibit substantially enhanced activity for the oxidation of carbon monoxide (CO) and methanol.[17] Herein, we present a side-by-side analysis of $SiO_x|Pt$ electrodes based thick (50 nm) and thin (3 nm) Pt substrates under identical test conditions, revealing significant differences in their physical and electrochemical properties. Of particular interest are differences in the $SiO_x|Pt$ buried interface, as probed by X-ray photoelectron spectroscopy (XPS) and cyclic voltammetry (CV). While XPS was used to monitor differences in the composition and structure of the Pt film at the buried interface, CV was employed to characterize the electrochemical properties of these electrodes in 0.5 M H_2SO_4 over narrow (non-oxidizing) and wide (oxidizing) ranges of applied potential. After reporting on differences in the structural and electrochemical properties of the buried interface that result from variations in the SiO_x and Pt layer thicknesses, we explore how these differences affect i.) SiO_x permeability to electroactive species and ii.) stability of the SiO_x overlayer during one hour of CV cycling. Overall, this study highlights the tunability of the MCEC architecture and reveals structure-property relationships that will be key to establishing a molecular-level understanding of electrocatalysis at buried interfaces.

II. Experimental methods

Electrode Fabrication- Monocrystalline p^+Si(100) degenerately doped wafers (Prime-grade p+Si, resistivity < 0.005 Ω cm, 500−550 μm thick, WRS materials) were used as flat, conductive substrates that were unresponsive to light. Titanium and platinum at 99.99% purity were sequentially deposited by electron-beam deposition under high vacuum (<6×10^{-8} Torr) without substrate heating to varying thicknesses at a rate of 0.5 and 1 Å s^{-1}, respectively. Thicknesses were monitored using a quartz crystal thickness monitor. Wafers were cleaved into 1.4 cm × 2.5 cm pieces and washed sequentially in acetone, methanol, isopropanol, and deionized water under sonication. A solution of trimethylsiloxy terminated polydimethyl-siloxane (PDMS) in toluene was spin coated onto the Pt|Ti|p^+Si substrates for 2.5 minutes at 4000 rpm. The SiO_x films having target thicknesses of 2.0, 5.0 and 10.0 nm were fabricated from PDMS/toluene solutions with concentrations of 1.2, 3.0 and 5.3 mg mL^{-1}, respectively. The PDMS-coated electrodes were dried in a vacuum oven at 80 °C for 1 hour before undergoing treatment in a UV ozone chamber for 2 hours (UVOCS, T10X10/OES) to convert the PDMS to SiO_x. An electrical contact was made by soldering a copper wire onto the back side of the silicon substrate using indium solder with a soldering iron temperature set to 218°C. The geometric area of the electrode was defined using 3M electroplater's tape, resulting in a circular 0.246 cm^2 opening on the front of the electrode through which the electrocatalytic surface was exposed to the electrolyte.

Materials Characterization- SiO_x overlayer thicknesses were measured using a J.A. Woollam alpha-SE ellipsometer. The thicknesses of SiO_x overlayers in the SiO_x|Pt|Ti|p^+Si samples were determined by sequentially fitting the raw data with an optical model that used optical constants and substrate thicknesses determined from fitting bare control samples lacking SiO_x. When analyzing SiO_x|Pt electrodes based on 50 nm thick Pt films, the Ti layer was not included in the model. Surface topography and roughness were measured with a Bruker Dimension Icon Atomic

Force Microscope (AFM) in air using a ScanAsyst silicon tip on a nitride lever silicon cantilever with a 25 nm tip radius. Measurements were performed in peak force nanomechanical mapping mode using a scan rate of 0.977 Hz, a spring force constant of 0.4 N m^{-1}, and a resonant frequency of 70 kHz.

XPS measurements were made with a Phi XPS system at pressures $< 2 \times 10^{-10}$ Torr using a monochromatic Al Kα source (15 kV, 20 mA) and a charge neutralizer. All samples are tilted to 57.4 degrees relative to the X-ray source. Multiplex spectra were fit using XPSPEAK software using Shirley's algorithm for background subtraction. All peaks were calibrated such that the Pt 4f 7/2 peaks were centered on 71.2 eV.[18] The thicknesses of SiO_x overlayers based on XPS measurements were calculated using an overlayer model, which is described in Section V of the electronic supplementary information (ESI). Atomic ratios were calculated using each element's atomic sensitivity factor (ASF).[19] ASFs used in overlayer calculations for the metallic elements in oxide compounds were computed by multiplying the ASF of the metallic element by the ratio of the atomic density of that element in the oxide to its density in a pure elemental state.

Electrochemical Measurements- Most electrochemical measurements were performed in deaerated 0.5 M sulfuric acid prepared from concentrated sulfuric acid (H_2SO_4, Certified ACS plus, Fischer Scientific) and 18 MΩ deionized water (Millipore, Milli-Q Direct 8). All electrochemical measurements were conducted with a SP-200 BioLogic potentiostat and carried out in a standard three-neck round bottom glass cell with a commercial Ag|AgCl (sat. 3 M KCl) reference electrode (E° = 0.228 V vs NHE, Hach, E21M002) and a Pt-mesh (Alfa Aesar, 99.9%) counter electrode. The electrolyte was deaerated by purging with nitrogen gas (N_2) for 20 minutes before experiments, while the headspace was continuously purged with N_2 for the

duration of all experiments. Current densities were normalized with respect to the geometric area of the exposed electrode.

Narrow window CV measurements were performed for 228 cycles (1 hr.) between 0.06 V and 0.82 V vs. RHE, and wide window CV measurements were performed for 151 cycles (1 hr.) between 0.06 V and 1.22 V vs. RHE, respectively. Upon completion of CV cycling experiments, electrodes to be analyzed by AFM and/or XPS were removed from the glass cell, gently rinsed with18 MΩ deionized water to remove residual electrolyte for ≈5 s, and dried under a stream of compressed N_2 gas. Copper (Cu) stripping voltammetry was carried out with sequential linear sweep voltammograms (LSVs) in solutions of 0.1 M H_2SO_4 (background) and 0.1 M H_2SO_4 with 2 mM $CuSO_4$ (Sigma-Aldrich, ReagentPlus Grade). For both LSV measurements, the electrode potential was held at +0.358 V vs. RHE for 50 seconds before sweeping the potential from +0.358 V to +1.0 V RHE at a scan rate of 100 mV s^{-1}. The difference in the integrated charge between the two curves was used to calculate the electrochemically active surface area (ECSA) of the electrode using a conversion factor of 420 μC cm^{-2} for polycrystalline Pt.[20]

III. Results and Discussion

3.1 Overview of SiO_x|Pt electrodes investigated in this study

A series of SiO_x|Pt electrodes of different overlayer thicknesses were synthesized from a PDMS precursor using a low temperature photochemical conversion process that has been described in detail elsewhere.[21,22] Briefly, a PDMS/toluene mixture was spin-coated onto the Pt thin film substrate, followed by evaporation of the solvent and subsequent conversion of PDMS to a continuous SiO_x overlayer within a UV-Ozone cleaning system. During this process, reactive oxygen species generated within the system convert methyl groups in the PDMS into gaseous CO_2 and H_2O byproducts, leaving behind amorphous SiO_x that is primarily comprised of SiO_2.

By adjusting the concentration of PDMS within the solvent mixture, precise control of the SiO_x thickness can be obtained. In this study, $SiO_x|Pt$ electrodes with SiO_x thicknesses between ≈1 nm and 10 nm were made on two different Pt substrates: (i.) a "thick", or bulk-like Pt film having a thickness of 50 nm (Figure 1a) and (ii.) a "thin" Pt thin having a thickness of 3 nm that was sequentially deposited onto a 2 nm thick Ti adhesion layer (Figure 1c). Within a set of samples, electrodes with three different SiO_x thicknesses (t_{SiOx}) were typically fabricated with target thicknesses of t_{SiOx} ≈ 2 nm, 5 nm, and 10 nm. Throughout this paper, the reported values of t_{SiOx} are those measured by ellipsometry, unless stated otherwise.

3.2 Characterization of SiO_x-encapsulated "thick" Pt films

Figure 1b shows a representative AFM image of an as-synthesized 4.8 nm thick SiO_x overlayer (t_{SiOx}=4.8 nm) deposited onto a 50 nm thick Pt substrate. The surface of the SiO_x electrode is very smooth, having a root mean squared (rms) roughness of 0.48 nm that represents a slight decrease from a value of 1.00 nm measured for the bare 50 nm Pt substrate lacking any SiO_x overlayer. AFM images show that no large cracks or holes the SiO_x overlayers are detected by AFM, although smaller pinholes (< 20 nm diameter) are observed for the $SiO_x|$(thick Pt) electrode with the thinnest SiO_x overlayer (t_{SiOx}=1.0 nm) (ESI Figure S1).

The thicknesses of SiO_x overlayers were determined by ellipsometry and are reported in Table I. Ellipsometry measurements show that the SiO_x overlayer thicknesses are extremely uniform across a given sample, with variations in t_{SiOx} across a large 3.5 cm^2 sample typically being less than 5% from the average thickness. As-made samples were also characterized by XPS to determine chemical and physical properties of buried interfaces located within a few nanometers of a sample surface. Multiplex scans of the Pt 4f, Si 2p, O 1s, C 1s, and Ti 2p regions were taken for as-made $SiO_x|Pt$ and bare Pt control samples. The Si 2p and C 1s spectra of

SiO_x|(thick Pt) electrodes are provided in the Figure S2, where it can be seen that the Si 2p peak centers for SiO_x|Pt samples correspond to Si in the +4 oxidation state (SiO_2) and small amounts of carbon (10-16 atomic %, excluding Pt signal) are present in/on all samples. Both findings are consistent with our previous studies of SiO_x produced by the UV ozone process.[7,14] The Si 2p and Pt 4f signals were also used to estimate the thicknesses of SiO_x overlayers from standard XPS overlayer models, which gave values of t_{SiOx} for the thinnest SiO_x overlayers within 0.2 nm of the values measured by ellipsometry.

Pt 4f spectra also provided useful information about the nature of Pt atoms at the SiO_x|Pt buried interface. Figure 2a shows the Pt 4f spectra for a 1.4 nm SiO_x|(thick Pt) sample and two bare 50 nm thick Pt control samples. The first control was an as-made, unmodified 50 nm thick Pt film ("0 nm SiO_x") that gives a standard Pt 4f spectra consistent with metallic Pt^0. The second control was a 50 nm thick bare Pt thin film that was treated for 2 hours in the UV ozone chamber ("UV ozone Pt"). Shoulders at higher binding energies are evident in the Pt 4f spectra for the UV ozone Pt control and 1.4 nm SiO_x|Pt samples, indicating the presence of Pt bound to oxygen, which is generically referred to as PtO_x throughout this paper. In order to isolate the Pt 4f signal associated with PtO_x species from metallic Pt^0, the Pt $4f_{7/2}$ peak intensities of the UV ozone Pt control and 1.4 nm SiO_x|(thick Pt) electrode were normalized to that of the untreated bare Pt control, after which the spectra of the latter was subtracted from that of the former to obtain Pt 4f difference spectra (Figure 2b). The PtO_x peaks in the Pt 4f difference spectra for the UV ozone treated bare Pt sample are shifted to higher binding energy (BE) compared to the SiO_x|(thick Pt) sample, indicating that the PtO_x species on the surface of that sample possess, on average, a higher oxidation state than those at the buried interface of the SiO_x|Pt sample. Both difference spectra contain multiple pairs of Pt 4f peaks, which were assigned to three different PtO_x species

based on previously reported Pt 4f peak centers for adsorbed oxygen on Pt (PtO$_{ad}$), Pt monoxide (PtO), and Pt dioxide (PtO$_2$).[23] Analysis of the fitted PtO$_x$ Pt 4f peak areas for these species indicates that the PtO$_x$ layer of the UV ozone-treated Pt control contains 14% PtO$_{ad}$, 42% PtO, and 44% PtO$_2$, while the PtO$_x$ interlayer at the buried interface of the 1.4 nm SiO$_x$|(thick Pt) sample contains 42% PtO$_{ad}$ and 58% PtO.

The presence of PtO$_x$ species at the buried interface of as-synthesized SiO$_x$|(thick Pt) electrodes was also verified by electrochemically reducing them during the first scan segment of cyclic voltammetry (CV) measurements in 0.5 M H$_2$SO$_4$. Immediately after immersing an electrode in the electrolyte, CV scans were initiated at a potential of 0.82 V vs. RHE, which is just below the onset potential for underpotential deposition (upd) of oxygen species. As the potential is scanned in the negative direction, broad peaks associated reduction of PtO$_x$ species are observed. The first CV scan for the untreated Pt control sample doesn't exhibit significant reduction current in the range of 0.3−0.8 V vs. RHE, confirming that there are negligible amounts of PtO$_x$ on that sample before initiating CV cycling. In contrast, the first CV cycles for the UV ozone treated bare Pt electrode and all of the SiO$_x$-encapsulated Pt electrodes possess distinct reduction peaks between ≈ 0.3 V and 0.7 V vs. RHE. Figure 3b shows that the PtO$_x$ reduction peaks are completely absent in the subsequent CV cycles, confirming that the PtO$_x$ species being reduced in the first cycle were not formed electrochemically but were present on the as-made samples as a result of the UV-ozone process.

The background-corrected charge associated with PtO$_x$ reduction during the first CV cycle, Q$_r$, was used to estimate the thicknesses of PtO$_x$ interlayers from Faraday's law. Assuming an average PtO$_x$ density of 14.1 g cm^{-3} (corresponding to that of PtO)[24] and an average Pt oxidation state of +2, PtO$_x$ thicknesses in the range of 2.2 Å − 6.6 Å were obtained (Table I).

11

Taking the lattice constant of the PtO_x layer to be 3.1 Å (similar to that of α-PtO_2 and PtO^{25}), the

PtO_x thicknesses determined from CV measurements correspond to $\approx$ 0.7- 2.1 atomic layers of

PtO_x. The slight decrease in PtO_x thickness for the 10.3 nm SiO_x overlayer may result from a

shielding effect whereby the thicker SiO_x overlayer suppresses oxidation of the underlying Pt

during the UV Ozone conversion process. Additionally, it should be noted that the CV scans in

Figure 3a possess significant differences in the PtO_x reduction onset potentials and peak centers,

which arise from differences in the kinetics and/or energetics of reducing various PtO_x species

back to the metallic Pt^0 state.[26] Comparing the PtO_x reduction peak centers for the series of

SiO_x|(thick Pt) electrodes, a shift to more negative potentials is observed with increasing SiO_x

overlayer thickness. This shift in peak potential may reflect differences in the PtO_x species that

are present at the buried interface, but could also be convoluted with differences in mass

transport constraints imposed by the presence of the SiO_x overlayers.

Figure 3b shows steady state CV curves obtained for the same SiO_x|Pt electrodes upon

extended CV cycling between 0.06 V to +0.82 V vs. RHE. Over this relatively narrow potential

range, none of the samples exhibit any features associated with the oxidation of Pt or formation

of upd oxygen. The major features in these CV curves are associated with the underpotential

deposition and desorption of hydrogen atoms, which are located between $\approx$ 0.0 V – 0.3 V RHE.

The integrated hydrogen upd (H_{upd}) signal is a measure of the electrochemically active surface

area (ECSA) of Pt electrocatalysts, and is seen to be greatly suppressed for the bare Pt control

sample compared to the SiO_x-encapsulated samples. The lower-than expected H_{upd} signal and

lack of sharp H_{upd} peaks for the bare Pt control are observations that are common for Pt

electrodes that are not flame annealed or scanned to potentials sufficient to oxidize Pt surface

atoms and adventitious impurity species that can suppress H adsorption.[26] In contrast, the 1.4 nm

and 4.6 nm SiO_x-encapsulated samples exhibit sharp H_{upd} features and integrated H_{upd} signals that are 100–130 % larger than that of the bare Pt control sample. The H_{upd} peaks for the t_{SiOx} = 10.3 nm $SiO_x|Pt$ sample are less pronounced and slightly skewed, which may be attributed to slow proton diffusion through the thicker SiO_x overlayer.[11]

When changes in the H_{upd} features are tracked as a function of cycle number (Figures S5-S8), it is seen that the CV signals for the bare Pt and t_{SiOx} =1.4 nm electrodes slowly shrink with increasing cycle number, while the H_{upd} signal actually increases for t_{SiOx} = 4.6 nm and 10.3 nm $SiO_x|Pt$ electrodes. The differences in H_{upd} behavior may be explained by the membrane-like properties of the SiO_x layers. If trace amounts of carbon-containing contaminants are present in the electrolyte and cannot be oxidized over the narrow potential CV window, they can poison exposed Pt surface atoms, thereby decreasing H_{upd} signal. We hypothesize that the SiO_x overlayer functions as a diffusion barrier that impedes transport of contaminants to the buried interface, thereby enabling sharp H_{upd} features that do not decrease with cycling.

CV cycling in deaerated 0.5 M H_2SO_4 was also performed on an identical set of $SiO_x|$(thick Pt) electrodes over a wider potential window that extended to +1.22 V vs. RHE (Figure 3c). Unlike the narrow window CV measurements of Figure 3b, all samples with t_{SiOx} < 10 nm produce CV curves in the wider window that possess sharp H_{upd} features that are characteristic of polycrystalline Pt electrodes in sulfuric acid.[26,27] The H_{upd} peak locations for the 1.4 nm $SiO_x|$(thick Pt) electrode remain consistent with those observed in Figure 3b, while the H_{upd} peaks for the 10.3 nm $SiO_x|$(thick Pt) electrode remain skewed due to slow proton diffusion through the SiO_x overlayer. Interestingly, some of the H_{upd} peak locations for the t_{SiOx} = 4.6 nm $SiO_x|$(thick Pt) electrode are very different from those observed for the t_{SiOx} = 1.4 nm $SiO_x|$(thick Pt) and bare Pt control electrodes (see ESI Figure S9a for a zoomed in view of H_{upd} features).

The most notable difference is the presence of prominent H_{upd} peaks in the CV curves of the t_{SiOx} = 4.6 nm SiO_x|(thick Pt) electrode that are centered around +0.26 V RHE. This H_{upd} peak location has been commonly associated with H_{upd} on Pt(100) terraces, while the H_{upd} peaks centered around +0.12 V RHE are predominantly associated with H_{upd} on Pt(110) and Pt(111) orientated surfaces.[27,28] This observation implies that the average Pt crystal orientation and/or crystalline defect densities at the SiO_x|Pt buried interface depend on the thickness of the SiO_x overlayer. It should be noted that the electrodes used for the CV measurements in Figure 3 were all made from a common Pt substrate, meaning that the differences in H_{upd} features are unlikely to be caused by differences in the initial crystal structures of as-made substrates.

At more positive potentials, the wide window CV scans in Figure 3c possess additional features associated with the oxidative adsorption of upd oxygen and formation of Pt oxides during the positive scan segment, as well as the subsequent reduction of PtO_x species during the negative scan segment. The PtO_x features of the bare Pt and 1.4 nm SiO_x|(thick Pt) electrodes are very similar, but the PtO_x oxidation and reduction peaks become much more pronounced with increasing thickness of the SiO_x overlayer. The increase in the total PtO_x signal for the thicker SiO_x overlayers is accompanied by a $\approx$ 100 mV shift in the onset of PtO_x formation to more negative potentials. A similar phenomenon has been reported for polycrystalline Pt electrodes encapsulated by ultrathin layers of atomic layer deposited (ALD) SiO_2, although no explanation was provided.[29] This negative shift in the PtO_x formation potential may be related to restructuring of the Pt surface, which could produce a higher percentage of crystal facets and/or defects that are more susceptible to oxidation. CV investigations of Pt single crystals in 0.5 H_2SO_4 have shown that Pt(100) electrodes exhibit a $\approx$ 50-100 mV shift in the PtO_x onset potential with respect to Pt(110) and Pt(111) electrodes.[27] This is consistent with our observation

that the thicker $SiO_x|Pt$ electrodes exhibiting more pronounced Pt(100) H_{upd} features simultaneously show a negative shift in the onset potential of PtO_x formation. However, these observations may also be related to confinement effects at the buried interface, where disruption of the electrochemical double layer[30] and/or interactions with the SiO_x overlayer[17] could cause the Pt at the buried interface to become more oxophilic (i.e. more easily oxidized). For example, it is well known that the formation of adsorbed OH and O species on Pt can be suppressed due to competitive adsorption of anions.[31] In this study, it is possible that SiO_x overlayers may affect Pt oxidation by making it more difficult for anions to reach the buried interface, thereby allowing the formation of PtO_x species at more negative potentials.

3.3 Characterization of SiO_x-encapsulated "thin" Pt electrodes

The results presented up until this point have focused on the effects of varying the thickness of the SiO_x overlayer on 50 nm "thick" Pt substrates, but it is also possible to tune the properties of MCECs by altering the composition of the metal layer. To demonstrate this, additional $SiO_x|Pt$ electrodes were prepared by depositing SiO_x overlayers onto "thin" Pt substrates consisting of sequentially deposited 3 nm of Pt on 2 nm of titanium (Ti).

Analysis of AFM images (Figure 1d and ESI Figure S1a) of the bare thin Pt substrates shows that they are even smoother than the thick Pt substrates, having a typical rms roughness of 0.26 nm. An inverse relationship between film roughness and thickness, as seen here, is commonly observed for various thin film growth methods.[32,33] The difference in rms roughness at the surface of thin and thick Pt samples decreases after coating the Pt substrates with equivalent thicknesses of SiO_x, but the larger difference in roughness of the bare substrates is likely to persist at the buried interface of $SiO_x|Pt$ electrodes. Close inspection of the AFM image of the 1.6 nm $SiO_x|$(thin Pt) sample (Figure S1b) reveals that it possesses numerous nanoscopic

holes, < 20 nm, similar to those identified for the thinnest SiO_x|(thick Pt) electrodes. However, the holes are no longer evident for t_{SiO_x} > 5 nm (Figure S1c).

Besides differing in their surface morphology, thick and thin Pt substrates were also found to vary in their composition due to the absence and presence, respectively, of Ti in close proximity to the front surface of the substrate. The source of the Ti is the adhesion layer deposited between inert $p^+Si(100)$ wafer and Pt thin film. One way that Ti may reach the front surface of thin Pt substrates is by alloying between Ti and Pt, which can occur during the e-beam deposition process. Evidence of alloying in e-beam Pt/Ti bilayers has previously been provided by cross-sectional transmission electron microscopy (TEM).[34] In the current study, significant Ti 2p signal in XPS measurements of as-deposited and UV ozone-treated bare Pt/Ti substrates (Figure 4a) give strong evidence of the presence of Ti in the near surface region of these samples. While no Ti 2p signal is observed for the thick Pt substrate, minor peaks associated with metallic Ti ($2p_{3/2}$ peak center at 454.1 eV) and larger peaks associated with a higher oxidation state ($2p_{3/2}$ peak center of 457.6 eV) are evident for the thin Pt substrate. Ti 2p signal is also seen for the thinnest SiO_x|(thin Pt) electrodes, although its intensity is greatly attenuated by screening from the SiO_x overlayer (Figure S3). The Ti 2p peaks at higher binding energy exhibit multiplex splitting of 5.6 eV, which is very similar to that of TiO_2, although the peak center binding energies are ≈ 1.2 eV lower.[18] These observations indicate that most of the Ti present near the surface has TiO_2-like character, although its XPS signature is not perfectly consistent with stoichiometric TiO_2. Interestingly, UV ozone treatment of the thin Pt substrate in the absence of any PDMS results in a ≈230% increase in the Ti 2p signal intensity and concomitant increase in the atomic ratio of Ti:Pt from 0.19 to 0.91. This result shows that Ti is drawn to the surface of the metal bilayer not only by alloying between the Pt and Ti layers, but also by the

16

highly oxidative UV ozone treatment. Given that i.) the UV ozone treatment time (2 hours) is

significantly longer than the e-beam deposition time and ii.) the formation of TiO_2 from its

elements has a very large thermodynamic driving force, it is likely that the UV ozone treatment

contributes the most to enrichment of Ti at the metal surface and SiO_x|Pt buried interfaces.

XPS characterization was also used to monitor differences in the PtO_x interlayer between

thin and thick Pt substrates, revealing substantially less PtO_x Pt 4f signal for samples based on

the former than the latter (Figure 4b). The absence of PtO_x signal is seen in the raw Pt 4f spectra,

as well as the Pt 4f difference spectra (Figure S4b) for the 2.1 nm SiO_x|(thin Pt) electrode. This

observation is consistent with previous studies showing that composite electrocatalysts based on

the combination of TiO_x and Pt group metals (or their oxides) such as Ru^{35} or Pt^{36} exhibit

enhanced resistance to oxidation and/or dissolution of the Pt group metal. In fact, Ti and TiO_2 are

crucial ingredients for dimensionally stable anodes (DSA®) that are frequently employed under

harsh oxidation conditions in various industrial electrochemical processes.[37] In this study, the

difference in PtO_x interlayer thickness for the thin and thick Pt substrates was confirmed by

analyzing the PtO_x reduction charge (Q_r) in the negative sweep of the first CV cycle in 0.5 M

H_2SO_4 (Figure 3a, 5a). The amounts of PtO_x in the SiO_x|(thin Pt) electrodes determined from

analysis of the CV curves were found to be 17 % -65 % lower than those present in to SiO_x|(thick

Pt) electrodes (Table I). These numbers indicate that sub-monolayer amounts of PtO_x, ≈0.25 to

0.97 atomic layers, are present at the buried interface of SiO_x|(thin Pt) electrodes. Besides having

lower Q_r, the PtO_x reduction features of the SiO_x|(thin Pt) electrodes also differed from those of

the SiO_x|(thick Pt) samples in that they were broader and showed little variation in the location of

the peak center (≈0.5 V vs. RHE) on t_{SiOx}. These differences in PtO_x reduction features in Figures

3a and 5a suggest that the thickness and redox properties of the PtO_x interlayers formed on the as-made electrodes depend not only on SiO_x thickness, but also the substrate.

SiO_x|(thin Pt) electrodes were also characterized by CV in 0.5 M H_2SO_4 over narrow (Figure 5b) and wide (Figure 5c) potential windows to compare their H_{upd} and PtO_x redox features to those of SiO_x|(thick Pt) electrodes. As shown in Figure 5b, the steady state narrow window CV curves of all SiO_x|(thin Pt) electrodes are all very similar to each other, with slightly larger H_{upd} signal than the bare thin Pt electrode. As with the SiO_x|(thick Pt) electrodes, we attribute the larger H_{upd} features for the SiO_x|Pt electrodes to the ability of the SiO_x overlayer to block impurities from reaching the buried interface. In comparing Figure 5b to Figure 3b, it is seen that H_{upd} features for the SiO_x|(thin Pt) electrodes are much less sharp than those of SiO_x|(thick Pt) electrodes, while their integrated H_{upd} signals are significantly smaller than those for SiO_x|(thick Pt) electrodes. The smaller H_{upd} signal may be partially explained by the lower rms roughness for electrodes based on thin Pt substrates, but could also result from a lower availability of upd sites at the buried interface due to the presence of Ti atoms that have segregated there after the UV-Ozone treatment.

CV measurements conducted over the wider CV range (Figure 5c) show that the integrated H_{upd} signal of SiO_x|(thin Pt) electrodes greatly increases compared to that measured over the narrow potential window, becoming comparable to those calculated for SiO_x|(thick Pt) electrodes. The similar H_{upd} signal intensities in wide window CVs indicates that differences in rms roughness can't be solely responsible for the lower H_{upd} signal of SiO_x|(thin Pt) electrodes over the narrow potential window, suggesting that differences in H_{upd} coverage and energetics at the buried interface might also be factors. In going from the narrow to wide scan window, the H_{upd} peaks for SiO_x|(thin Pt) electrodes also become much sharper, with peak locations that don't deviate substantially from those of SiO_x|(thick Pt) electrodes. Despite similarities in H_{upd} features

over the wide scan range, notable differences in PtO_x redox features persist at more positive potentials. In particular, the $SiO_x|(thin\ Pt)$ electrodes show less pronounced PtO_x features than the bare thin Pt control (Figure 5c), while $SiO_x|(thick\ Pt)$ electrodes showed larger PtO_x features than the thick Pt control (Figure 3c). Increasing the SiO_x thickness on thin Pt substrates leads to a small negative shift in the onset potential of PtO_x formation and concomitant increase in PtO_x reduction charge, but these changes are much less pronounced than they were for the $SiO_x|(thick\ Pt)$ electrodes in Figure 3c. Overall, a comparison of the CVs in Figures 3c and 5c indicates that the $SiO_x|(thin\ Pt)$ electrodes are less prone to electrochemical formation of PtO_x at the buried interface than those made from the thicker 50 nm Pt substrate.

3.4 Substrate effects on transport of electroactive species through SiO_x overlayers

Understanding the transport properties of MCEC overlayers is of great importance for several reasons. First and foremost, the permeabilities of reactants and products through the overlayer must be sufficiently high to avoid large concentration gradients and associated concentration overpotentials. These permeabilities, combined with the desired operating current density and the bulk concentrations of the reactant, set the maximum overlayer thickness that can be used before significant concentration overpotential losses are incurred.[12] Transport properties of the overlayer are also important because differences in permeabilities of electroactive species can be leveraged to control reaction selectivity or poison resistance.[11] Understanding the structure-property relationships that control transport of electroactive species through overlayers is therefore a key aspect of developing design rules needed for tuning the properties of MCECs.

In this study, the transport of electroactive Cu^+ and H^+ through SiO_x overlayers was investigated for $SiO_x|Pt$ electrodes based on the thin and thick Pt substrates. The ability of Cu^{2+} to transport through the SiO_x overlayers and reach the $SiO_x|Pt$ buried interface was viewed by

performing Cu stripping voltammetry in an electrolyte containing 2 mM $CuSO_4$ and 0.1 M H_2SO_4. In these measurements, electrodes were first held at a potential of 0.358 V vs. RHE for 50 s, during which time Cu^{2+} ions deposit on accessible Pt atoms by under potential deposition. At this potential, only a single layer of Cu can adsorb, making this technique useful for measuring the ECSA of electrocatalysts. Next, the potential was swept from +0.358 V to +1.0 V vs. RHE, resulting in oxidative stripping of upd Cu. An identical linear sweep voltammetry (LSV) curve was also carried out in the 0.1 M H_2SO_4, shown in Figure S10, and the difference between the two LSV curves integrated to determine the total amount of Cu_{upd} stripped from the surface. Figures 6a (for thin Pt substrates) and 6b (for thick Pt substrates) contain the Cu stripping difference curves of $SiO_x|Pt$ electrodes. Consistent with our recent study on $SiO_x|$(thin Pt) electrodes,[11] the Cu stripping curves in Figure 6a exhibit negligible Cu_{upd} oxidation signal, indicating that Cu^{2+} is not able to penetrate through SiO_x overlayers deposited on the thin 3 nm Pt substrates. However, significant Cu stripping signal is observed for $SiO_x|$(thick Pt) electrodes. A comparison of the integrated Cu_{upd} signal (Figure 6c) reveals that the $SiO_x|Pt$ electrodes based on the thick Pt substrate show a $\approx$ 1.5 - 6 fold increase in Cu_{upd} signal relative to the $SiO_x|$(thin Pt) electrodes. This finding suggests that a greater fraction of sites at the buried interface of $SiO_x|$(thick Pt) electrodes are electrochemically accessible to Cu^{2+}, and may be explained by a higher permeability of Cu^{2+} through the SiO_x deposited on thick Pt. It is also interesting to note that the shape of the Cu stripping signal for the $SiO_x|$(thick Pt) samples deviates greatly from the bare Pt substrates, with most signal shifted to higher potentials, indicating a higher binding energy and different energetics of the Cu_{upd} at $SiO_x|Pt$ interfacial sites compared to the bare Pt surface.

The greatly suppressed ECSAs of $SiO_x|Pt$ electrodes based on Cu stripping (Figure 6) contrasts with the large H_{upd} features seen in CV curves in 0.5 M H_2SO_4 (Figures 3 and 5) that indicated relatively high coverages of H_{upd} at the $SiO_x|Pt$ buried interface sites for both thick and thin Pt substrates. However, the CVs used to measure H_{upd} features do not require high fluxes of protons. To better compare the rates of proton transport, the hydrogen evolution reaction (HER) properties of $SiO_x|Pt$ electrodes were evaluated by LSV measurements from 0.82 V to -0.38 V vs. RHE in dearated 0.5 M H_2SO_4 after 1 hour of CV cycling between 0.06 V and 0.82V vs. RHE (Figure 7). It should be noted that the LSV curves for the thin and thick bare Pt control samples overlap almost perfectly, indicating that the presence of any Ti in the former has negligible effect on the intrinsic HER activity of these SiO_x-free samples. Thus, the differences in the LSV curves in Figure 7 for the $SiO_x|$(thin Pt) and $SiO_x|$(thick Pt) electrodes must arise from differences in the SiO_x overlayers and/or their buried interface with the underlying Pt. Although it is possible that changing SiO_x overlayer thickness could lead to slight changes in the HER reaction energetics at the buried interface, the monotonic decrease in current density with increasing SiO_x thickness is most likely a result of concentration overpotential losses that develop across the SiO_x overlayers.[11] By extension, we interpret the differences in the LSV curves for the $SiO_x|$(thin Pt) electrodes (Fig. 7a) and $SiO_x|$(thick Pt) electrodes (Fig. 7b) to be a result of differences in the permeabilities of protons diffusing through the SiO_x overlayers. The weaker thickness-dependence of the LSV curves of the $SiO_x|$(thick Pt) electrodes can be attributed to a higher permeability for protons, consistent with the higher permeability for Cu^{2+} ions that was seen in Figure 6b.

Consistent with our previous study,[11] he LSV curves of the $SiO_x|$(thin Pt) electrodes exhibit a strong dependence on t_{SiOx}, with large overpotentials evident for t_{SiOx} =4.8 nm and t_{SiOx}

=7.9 nm. However, the SiO$_x$|Pt electrodes based on the thick Pt substrates exhibit almost no difference in the LSV curves for SiO$_x$ thicknesses of 5 nm or less (Figure 7b). A side-by-side comparison of the overpotentials at -20 mA cm^{-2} are provided in Figure 7c, showing that larger HER overpotentials are required for SiO$_x$|Pt electrodes made from the thin bilayer Pt/Ti substrates. Our previous study showed that the additional HER overpotentials incurred by SiO$_x$-encapsulation can be modeled as concentration overpotentials associated with transport of H$^+$/H$_2$ species across the SiO$_x$ overlayer.[11] By extension, we hypothesize that the differences in the LSV curves in Figures 6a and 6b are explained by lower permeability of protons through the SiO$_x$ overlayers deposited on thin Pt substrates compared to SiO$_x$ deposited on thick Pt substrates.

In evaluating the combined results of the Cu stripping voltammetry (Figure 6) and H$_2$ evolution (Figure 7) measurements, we find that transport of both H$^+$ and Cu^{2+} through SiO$_x$ overlayers is much more suppressed for SiO$_x$ overlayers deposited on thin Pt substrates than those deposited on thick Pt substrates. Although the exact origins of these "substrate effects" on the electrochemical properties of SiO$_x$|Pt electrodes are not obvious, the stark differences in behavior of the SiO$_x$(thin Pt) and SiO$_x$(thick Pt) electrodes highlight the wide range of properties that are accessible with the MCEC architecture.

3.5 Stability of SiO$_x$|Pt electrodes during CV cycling in sulfuric acid

In order for the overlayer of an MCEC to protect the encapsulated electrocatalyst, it is imperative that the overlayer itself also be stable under the operating conditions of interest. Takenaka *et al.* reported that SiO$_2$-encapsulated Pt nanoparticles used for the oxygen reduction reaction (ORR) showed minimal loss in ECSA and no noticeable changes in the silica layers after CV cycling for 20,000 cycles in 0.1 M HClO$_4$ between 0.0 V and 1.2 V vs. RHE.[7] Recent studies from our lab showed that UV ozone SiO$_x$-encapsulated Pt nanoparticle[8] and 3 nm Pt thin film[11] electrodes

exhibit stable performance as HER electrocatalysts in 0.5 M H_2SO_4. However, our more recent study investigating $SiO_x|$(thick Pt) planar electrodes for alcohol oxidation indicated partial delamination of the SiO_x overlayer during extended CV cycling in 0.5 M methanol + 0.5 M H_2SO_4.[17] None of the aforementioned studies provided detailed physical characterization of the SiO_x overlayers after extended operation. To better investigate the stability of SiO_x coatings under CV cycling as a part of the current study, AFM, ellipsometry, and XPS were used to monitor changes in the properties of $t_{SiOx} \approx 1$ nm and $t_{SiOx} \approx 5$ nm $SiO_x|$Pt electrodes resulting from CV cycling in 0.5 M H_2SO_4 over both narrow (0.06 – 0.82 V RHE) and wide (0.06 – 1.22 V RHE) potential scan ranges.

Representative AFM images of $SiO_x|$Pt electrodes in their initial state and after CV cycling are provided for two different SiO_x thicknesses for both thin (Figure 8a) and thick (Figure 8b) Pt substrates. For reference, AFM images of as-made bare Pt substrates are also provided. Looking first at Figure 8a, AFM is not able to detect any significant differences in the morphology of the $SiO_x|$(thin Pt) electrodes after CV measurements, with the exception of subtle coarsening of the t_{SiOx}=4.8 nm $SiO_x|$(thin Pt) electrode after CV cycling over the wide potential window. AFM images in Figure 8b show that the t_{SiOx}=1.0 nm $SiO_x|$(thick Pt) electrodes also maintain their original morphology after CV cycling over both short and wide windows. In contrast, the surfaces of the t_{SiOx}=4.8 nm $SiO_x|$(thick Pt) electrodes clearly changed after CV cycling in both the narrow and wide potential ranges, exhibiting morphologies that closely resemble the morphology of the bare thick Pt substrate. Rms roughness values computed for each sample (Figure 8c) support these qualitative descriptions, showing that negligible changes in surface roughness were observed for all samples except the t_{SiOx}=4.8 nm $SiO_x|$(thick Pt) electrodes. After both narrow and wide window CV cycling, the rms roughness of those

electrodes nearly doubled. The exact rms roughness values obtained from the post CV AFM images of the t_{SiOx}=4.8 nm SiO$_x$|(thick Pt) electrodes is very similar to that of the bare Pt substrate, indicating that most, but not all of the SiO$_x$ has been removed. Ellipsometry also indicated a substantial reduction in t_{SiOx} occurred for the 4.8 nm SiO$_x$|(thick Pt) electrode after CV cycling (Figure S16).

To further probe changes in the chemical and/or electronic properties of the SiO$_x$ overlayer and SiO$_x$|Pt buried interface caused by CV cycling, XPS was used to characterize the same t_{SiOx}=1.0 nm SiO$_x$|(thick Pt) and t_{SiOx}=1.6 nm SiO$_x$|(thin Pt) electrodes. Changes in the Si 2p, O 1s, and C 1s spectra relative to as-made electrodes are seen for both electrodes, but are most noticeable for the SiO$_x$|(thick Pt) electrode. As seen in Figure S11, notable positive shifts are seen in the Si 2p (0.40-0.82 eV), O 1s (0.67-0.89 eV), and C 1s spectra (0.42-0.76 eV), with the largest shifts seen for the SiO$_x$|(thick Pt) electrode that underwent CV cycling over the narrow potential window. The positive shifts in the Si 2p spectra could be explained by conversion of SiO$_x$ to a highly hydroxylated layer containing many silanol groups,[38] which would not be surprising given that the permeable SiO$_x$ overlayers were operated in an acidic electrolyte with pH below the pKa values of SiOH groups.[39] Also of interest in Figure S11 is the O 1s spectra of the SiO$_x$|(thick Pt) electrode taken after narrow window CVs, for which the O 1s peak center shifts by +0.8 eV to a binding energy of 532.4 eV. O 1s binding energies greater than those of the parent oxide have commonly been associated with hydroxylated oxides.[40–42] Thus, the O 1s spectra in Figure S11b may provide evidence that the SiO$_x$ overlayers deposited on the thick Pt substrates are themselves transformed to a highly hydroxylated and/or hydrated form during CV cycling. Volume expansion compared to the as-made sample would be expected to accompany such a transformation to a hydrated phase. Supporting this possibility, ellipsometry

measurements performed on the 1.0 nm SiO_x|(thick Pt) electrode after CV cycling indicate that t_{SiOx} increased to 4.5 nm. This increase in overlayer thickness may indicate swelling of the overlayer, perhaps due to hydration, but could also result from chemical and/or structural transformations that alter the optical properties of the SiO_x, and therefore the *apparent* thickness of the overlayer. In contrast, much smaller shifts are observed for the Si 2p (0.01 – 0.30 eV) and O 1s (-0.10-0.23 eV) spectra of the t_{SiOx}=1.6 nm SiO_x|(thin Pt) electrodes, with post-CV ellipsometry measurements, indicating that little-to-no change in SiO_x thickness had occurred from its as-synthesized state. However, one notable change in the SiO_x|(thin Pt) electrodes was seen for the electrode that underwent CV cycling over the wide potential window; after CV cycling, the Ti 2p signal almost completely disappears (Figure S12e), meaning that most of the TiO_x near the buried interface had leached from the buried interface.

Si 2p and Pt 4f spectra were also used to monitor changes in the Si:Pt atomic ratio resulting from CV cycling (Figure S15), which can be a useful measure of changes in the SiO_x overlayer thickness. While the Si:Pt atomic ratio of the 1.0 nm SiO_x|(thick Pt) electrodes decreased from ≈ 5.4 to 3.3 after both CV experiments, a moderate increase from Si:Pt ≈ 3.3 to 4.6 was calculated for the 1.6 SiO_x|(thin Pt) electrode after the narrow window CV scan. However, the atomic Si:Pt ratio was found to decrease from ≈ 3.3 to 2.2 for the SiO_x|(thin Pt) electrode after the wide window CV scan. XPS measurements performed on the 4.8 nm SiO_x|(thick Pt) (Figure S13) and 4.8 nm SiO_x|(thin Pt) (Figure S14) electrodes before and after CV cycling similarly reveal much better stability of SiO_x overlayers deposited on the thin Pt substrates. As evidenced by the nearly complete absence of Si 2p signal (Figure S13c) and dramatic reduction in the Si:Pt atomic ratio (Figure S15), XPS measurements confirmed that CV cycling over both potential ranges almost completely removed the thicker 4.8 nm SiO_x overlayers from the thick Pt substrates. On the other hand, the thicker 4.8 nm SiO_x|(thin Pt)

electrodes still maintain similar Si:Pt atomic ratios (Figure S15) after CV cycling, consistent with

AFM and ellipsometry measurements that had indicated the SiO_x overlayers remained well-

adhered to the thin Pt substrates. It is difficult to quantitatively assess changes in the SiO_x

thickness based on the Si:Pt atomic ratios due to possible film swelling and/or differences in

screening from adventitious species. Nonetheless, the absence of extremely large changes in

these ratios or in the intensities of the raw Si 2p spectra confirm that the electrodes based on the

thinnest SiO_x overlayers remain primarily intact, albeit with varying degrees of change to the

SiO_x composition.

To see whether or not chemical dissolution contributed to the decrease in SiO_x overlayer

thickness for the $\approx$ 5 nm SiO_x|(thick Pt) electrode, the thickness of a freshly made 5.3 nm

SiO_x|(thick Pt) sample was measured by ellipsometry before and after soaking in 0.5 M H_2SO_4.

After 20 hours of soaking, the measured SiO_x thickness decreased by less than 0.2 nm ($\approx$ 3% of

total film thickness). This result indicates that chemical dissolution should not influence SiO_x

stability over the timescale employed for the electrochemical CV measurements ($\approx$ 1 hour).

Given that considerable losses in overlayer thickness were observed for this same sample type

after 1 hour of CV cycling, our findings suggest that the primary mechanism of SiO_x overlayer

loss on the thick Pt substrates is delamination rather than dissolution. AFM images, ellipsometry,

and XPS measurements collectively show that the durability of SiO_x|Pt electrodes depends

strongly on both the SiO_x overlayer thickness and the choice of substrate.

3.6 Effects of PtO_x and Ti on the SiO_x|Pt buried interface

Several differences between the "thick" and "thin" Pt substrates may alter the structure-property

relationships of the SiO_x overlayer and SiO_x|Pt buried interface of SiO_x|Pt electrocatalysts. These

include differences in the substrate roughness, substrate crystallinity, thickness of the PtO_x

interlayer, and the presence of Ti-species (e.g. TiO_x, Pt_xTi_y) near the buried interface. The amount of PtO_x and presence of Ti appear to be especially important for explaining many key differences in electrochemical properties of $SiO_x|$(thick Pt) and $SiO_x|$(thin Pt) electrodes. XPS and CV measurements showed that the thickness of the PtO_x is significantly reduced for $SiO_x|$(thin Pt) electrodes, for which Ti originating from the adhesion layer may diffuse to the near-surface region and serve as an oxygen getter that suppresses PtO_x formation. Combining the influence of Ti with the shielding effect of the SiO_x overlayer during the UV ozone process, the $SiO_x|Pt|Ti$ electrodes presented in this study offer two control knobs for adjusting the thickness of the PtO_x interlayer. The relationships between SiO_x thickness, substrate type (thin or thick Pt), and the amount of the PtO_x interlayer (using Q_r as a proxy) are shown in Figure 9a. This figure shows that the amount of PtO_x is most sensitive to the choice of substrate, or rather, the presence of Ti. This relationship between the presence of Ti and PtO_x thickness is illustrated schematically in Figure 9, which shows a molecular-level view of as-made $SiO_x|$(thin Pt) (Fig. 9b) and SiO_x (thick Pt) (Fig. 9c) electrodes based on knowledge gained from XPS and CV measurements.

Figure 9 highlights structural differences at the $SiO_x|Pt$ buried interface of *as-made* electrodes, but it is not trivial to relate these structural characteristics to the electrochemical properties of $SiO_x|Pt$ electrodes. PtO_x interlayers formed during the UV ozone process are reduced during the first scan segment of the first CV scan, meaning that the structure(s) of the buried interface during and after operation are very likely to deviate from that of the as-made electrode. Nonetheless, we hypothesize that the initial thickness and composition of PtO_x interlayers can greatly influence the physical and chemical characteristics of the buried interface during operation. Reduction of a relatively thick PtO_x layer to form a more compact Pt layer can be expected to break bonds between PtO_x and the SiO_x overlayer, leading to a loosely connected

buried interface. Accordingly, reduction of thicker PtO_x interlayers is more likely to alter Pt crystal structure (e.g. reconstruction, defects, roughness) and/or the steric environment associated with nano-confined spaces at the buried interface compared to the initial state. On the other hand, an as-made $SiO_x|Pt$ electrode that possesses negligible PtO_x is more likely to maintain many of the original bonding interactions between the substrate and overlayer, minimizing structural changes at the buried interface.

In this study, differences in the electrochemical properties of $SiO_x|Pt$ electrodes were seen in the form of shifts in H_{upd} peaks, large variations in Cu_{upd} stripping features, shifts in PtO_x formation onset potentials, alterations in HER LSV curves, and variability in overlayer stability after CV cycling. Many of the finer details of the relationships between these observed properties and structural characteristics of $SiO_x|Pt$ electrodes remain ambiguous, but some details have emerged. In general, our measurements indicate that SiO_x overlayers deposited on thin Pt substrates exhibit better stability than SiO_x overlayers deposited on thick Pt substrates, and we primarily attribute this to differences in initial PtO_x interlayers that affect adhesion between the overlayer and substrate. The detrimental role of the PtO_x interlayer was verified with CV scanning over wide windows for the $SiOx|(thin Pt)$ electrodes, which can promote electrochemical formation of PtO_x. The presence/absence of PtO_x at the buried interface of as-made electrodes also correlates strongly with electrochemical characteristics such the location and magnitude of H_{upd} and Cu_{upd} features. These dependencies are attributed to differences in the Pt crystal structure and/or energetics of adsorbates located at the buried interface. Needless to say, a more detailed molecular-level understanding of the processing-structure-property relationships would be invaluable for tuning the catalytic properties of MCECs.

While this study has presented several new insights into the structure-property relationships of SiO$_x$|Pt electrocatalysts, many open questions remain. The presence of Ti species appears to indirectly affect the buried interface by altering the thickness of PtO$_x$ interlayers, but it remains to be seen whether TiO$_x$ may also directly impact structural and electrocatalytic properties of the buried interface. For example, it is unclear whether Ti species at the buried interface bonds with SiO$_x$, thereby creating robust "anchor points" between the overlayer and substrate that can promote adhesion and enhance confinement effects at the buried interface. A related question pertains to the influence of the metal oxide species (PtO$_x$ and TiO$_x$) on the structure-property relationships of the SiO$_x$ overlayer. This study showed that the morphological, chemical/electronic, and electrochemical characteristics of the SiO$_x$ overlayer were strongly affected by use of the thin or thick Pt substrate. In particular, stark differences in the Cu$_{upd}$ stripping voltammetry and H$_2$ evolution performance were observed, indicating that the permeabilities of the SiO$_x$ overlayers for Cu^{2+} and H$^+$ were greatly altered by changing the substrate. An explanation for the differences in permeabilities may be found in XPS characterization of SiO$_x$ films after CV cycling, which suggested that the SiO$_x$ overlayer deposited on the thick Pt substrate becomes significantly hydroxylated, while that deposited on the thin Pt substrate is better able to retain its initial, less hydroxylated state. Previous studies have indicated that proton transport through silica is facilitated by a "hydrogen hopping", or Grotthuss-type mechanism involving transfer of protons between silanol groups in silica.[43,44] If true, then one would expect to see substantially higher proton transport rates for the more heavily hydroxylated SiO$_x$|(thick Pt) electrodes; based on the HER measurements in Figure 7, this is exactly what was seen. Additional supporting evidence of differences in the overlayer composition was obtained from contact angle (θ_c) measurements of as-made ≈5 nm SiO$_x$|(thin Pt)

and SiO_x|(thick Pt) samples (Figure S17). These measurements showed that the SiO_x|(thick Pt) samples (θ_c =64.8 +/- 1.1°) are significantly more hydrophilic than the SiO_x|(thin Pt) samples (θ_c =79.9 +/- 1.7°), suggesting that there are differences in the chemical and/or physical properties of as-made overlayers that result from being deposited on different substrates. The smaller contact angle for the SiO_x|(thick Pt) sample is consistent with the SiO_x coating being more hydrated and/or hydroxylated than its SiO_x|(thin Pt) counterpart. However, a detailed mechanistic understanding of how the substrate impacts SiO_x structural and/or compositional characteristics that dictate its propensity to become hydroxylated, and therefore its ability to support cation transport, is lacking. With the aim of answering this and other fundamental questions about the structure-property relationships of oxide-encapsulated electrocatalysts, we expect that the use of *in situ* spectroscopies, aided by *ab initio* simulation tools, will be invaluable.[42]

3.7 Conclusions

The structure-property relationships governing the performance of MCECs based on oxide-encapsulated metals are significantly different, and in many ways, more complex than those that govern the performance of conventional "exposed" electrocatalysts. In order to uncover some of these relationships, this study has examined the physical, chemical, and electrochemical properties of model SiO_x-encapsulated Pt thin film electrodes, with a particular emphasis placed on characterizing the SiO_x|Pt buried interface. Through a combination of physical, spectroscopic, and electroanalytical characterization techniques, it was found that Pt oxide (PtO_x) interlayers are located at the buried interface of as-made samples, and that the thickness and composition of these interlayers can be tuned by adjustments in the thicknesses of the SiO_x overlayer and a Pt/Ti bilayer substrate. Importantly, the presence and amount of PtO_x interlayers in SiO_x|Pt electrodes, whether present initially or formed during electrochemical measurements, are found to correlate

with electrochemical properties such as upd adsorption/desorption features, HER performance, and stability of SiO_x overlayers. The large variations in electrochemical properties observed over the parameter space investigated in this study highlights the large degree of tunability afforded by the encapsulated electrocatalysts. Although many fundamental questions about the operation of encapsulated electrocatalysts remain, the structure-property relationships reported here represent a step forward in the development of design rules for this tunable class of emerging electrocatalysts. As the complex design rules governing the performance of oxide-encapsulated electrocatalysts are further refined through additional experimental and computational investigations, we expect that this emerging electrocatalyst architecture will be extended to many other materials and electrochemical reactions.

Acknowledgments

V. References

1   J. Greeley and N. M. Markovic, *Energy Environ. Sci.*, 2012, **5**, 9246–9256.

2   S. Gu, B. Xu and Y. Yan, *Annu. Rev. Chem. Biomol. Eng.*, 2014, **5**, 429–54.

3   Z. W. Seh, J. Kibsgaard, C. F. Dickens, I. Chorkendorff, J. K. Nørskov and T. F. Jaramillo, *Science (80-.).*, 2017, **355**, 146–+.

4   P. J. Ferreira, G. J. la O', Y. Shao-Horn, D. Morgan, R. Makharia, S. Kocha and H. A. Gasteiger, *J. Electrochem. Soc.*, 2005, **152**, A2256.

5   K. Maeda, K. Teramura, D. Lu, N. Saito, Y. Inoue and K. Domen, *Angew. Chemie - Int. Ed.*, 2006, **45**, 7806–7809.

6   H. Matsumori, S. Takenaka, H. Matsune and M. Kishida, *Appl. Catal. A Gen.*, 2010, **373**, 176–185.

7   S. Takenaka, H. Miyamoto, Y. Utsunomiya, H. Matsune and M. Kishida, *J. Phys. Chem. C*, 2014, **118**, 774–783.

8   N. Y. Labrador, X. Li, Y. Liu, H. Tan, R. Wang, J. T. Koberstein, T. P. Moffat and D. V. Esposito, *Nano Lett.*, 2016, **16**, 6452–6459.

9   B. Endr, N. Simic, M. Wildlock and A. Cornell, 2017, **234**, 108–122.

10   M. Qureshi, T. Shinagawa, N. Tsiapis and K. Takanabe, , DOI:10.1021/acssuschemeng.7b01704.

11   N. Y. Labrador, E. L. Songcuan, C. De Silva, H. Chen, S. J. Kurdziel, R. K. Ramachandran, C. Detavernier and D. V. Esposito, *ACS Catal.*, 2018, **8**, 1767–1778.

12   D. V. Esposito, *ACS Catal.*, 2018, **8**, 457–465.

13   A. T. Garcia-Esparza, T. Shinagawa, S. Ould-Chikh, M. Qureshi, X. Peng, N. Wei, D. H. Anjum, A. Clo, T. C. Weng, D. Nordlund, D. Sokaras, J. Kubota, K. Domen and K. Takanabe, *Angew. Chemie - Int. Ed.*, 2017, **56**, 5780–5784.

14   A. D. Doyle, J. H. Montoya and A. Vojvodic, *ChemCatChem*, , DOI:10.1002/cctc.201402864.

15   Y. Fu, A. V. Rudnev, G. K. H. Wiberg and M. Arenz, *Angew. Chemie - Int. Ed.*, 2017, **56**, 12883–12887.

16   H. Li, J. Xiao, Q. Fu and X. Bao, *Proc. Natl. Acad. Sci.*, 2017, **114**, 5930–5934.

17   J. E. Robinson, N. Y. Labrador, H. Chen, B. E. Sartor and D. V. Esposito, *(Under Rev.*

18   J. F. Moulder, W. F. Stickle, P. E. Sobol and K. D. Bomben, *Handbook of X-ray Photoelectron Spectroscopy*, Physical Electronics, Inc., Eden Prairie, MN, 1995.

19   C. D. Wagner, L. E. Davis, M. V Zeller, J. A. Taylor, R. H. Raymond and L. H. Gale,

Surf. Interface Anal., 1981, **3**, 211–225.

20 K. Varga, P. Zelenay and A. Wieckowski, *J. Electroanal. Chem.*, 1992, **330**, 453–467.

21 C. Mirley and J. Koberstein, *Langmuir*, 1995, **11**, 0–3.

22 M. Ouyang, C. Yuan, R. J. Muisener, a. Boulares and J. T. Koberstein, *Chem. Mater.*, 2000, **12**, 1591–1596.

23 K. S. Kim, N. Winograd and R. E. Davis, *J. Am. Chem. Soc.*, 1971, **93**, 6296–6297.

24 D. R. Lide, Ed., in *CRC Handbook of Chemistry and Physics, Internet Version*, CRC Press, Boca Raton, FL, 2005, pp. 4–75.

25 J. R. McBride, G. W. Graham, C. R. Peters and W. H. Weber, *J. Appl. Phys.*, 1991, **69**, 1596–1604.

26 V. Climent and J. M. Feliu, *J. Solid State Electrochem.*, 2011, **15**, 1297–1315.

27 K. Yamamoto, D. M. Kolb, R. Kotz and G. Lehmpfuhl, *J. Electroanal. Chem.*, 1979, **96**, 233–239.

28 N. Furuya and S. Koide, *Surf. Sci.*, 1989, **220**, 18–28.

29 G. Yuan, A. Agiral, N. Pellet, W. Kim and H. Frei, *Faraday Discuss.*, 2015, **176**, 233–249.

30 L. Bellarosa, R. García-Muelas, G. Revilla-López and N. López, *ACS Cent. Sci.*, 2016, **2**, 109–116.

31 B. E. Conway, *Prog. Surf. Sci.*, 1995, **49**, 331–452.

32 T. Aaltonen, M. Ritala, T. Sajavaara, J. Keinonen and M. Leskela, *Chem. Mater.*, 2003, **15**, 1924–1928.

33 J. Singh and D. E. Wolfe, *J. Mater. Sci.*, 2005, **40**, 1–26.

34 D. V. V Esposito, I. Levin, T. P. P. Moffat and a A. A. Talin, *Nat. Mater.*, 2013, **12**, 562–568.

35 L.-Å. Näslund, C. M. Sánchez-Sánchez, Á. S. Ingason, J. Bäckström, E. Herrero, J. Rosen and S. Holmin, *J. Phys. Chem. C*, 2013, **117**, 6126–6135.

36 E. Ding, K. L. More and T. He, *J. Power Sources*, 2008, **175**, 794–799.

37 S. Trasatti, *Electrochim. Acta*, 2000, **45**, 2377–2385.

38 T. L. Barr, *Appl. Surf. Sci.*, 1983, **15**, 1–35.

39 M. Sulpizi, M. P. Gaigeot and M. Sprik, *J. Chem. Theory Comput.*, 2012, **8**, 1037–1047.

40 S. Yamamoto, H. Bluhm, K. Andersson, G. Ketteler, H. Ogasawara, M. Salmeron and A.

Nilsson, *J. Phys. Condens. Matter*, 2008, **20**, 184025.

41   S. Benkoula, O. Sublemontier, M. Patanen, C. Nicolas, F. Sirotti, A. Naitabdi, F. Gaie-Levrel, E. Antonsson, D. Aureau, F. X. Ouf, S. I. Wada, A. Etcheberry, K. Ueda and C. Miron, *Sci. Rep.*, 2015, **5**, 1–11.

42   T. A. Pham, X. Zhang, B. C. Wood, D. Prendergast, S. Ptasinska and T. Ogitsu, *J. Phys. Chem. Lett.*, 2018, **9**, 194–203.

43   M. Nogami, R. Nagao and C. Wong, *J. Phys. Chem. B*, 1998, **102**, 5772–5775.

44   J. C. Fogarty, H. M. Aktulga, A. Y. Grama, A. C. T. van Duin and S. A. Pandit, *J. Chem. Phys.*, 2010, **132**, 174704.

Graphical abstract:
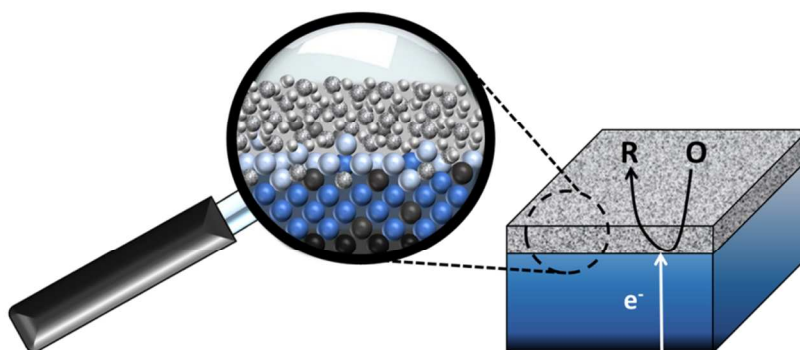
Tables and Figures

Table I. Thicknesses of SiO_x and PtO_x layers on as-made electrodes. SiO_x thicknesses were determined by ellipsometry, while PtO_x thicknesses were calculated based on the charge associated with electrochemical PtO_x reduction, as described in the text. (*) Indicates bare Pt control samples that were treated in the UV ozone chamber without any PDMS.

Substrate	SiOx Thickness / nm	PtOx Thickness / nm
Thin Platinum (2 nm Ti | 3 nm Pt)	0	0.00
	0*	0.03
	1.58	0.30
	4.76	0.21
	7.88	0.08
Thick Platinum (1 nm Ti | 50 nm Pt)	0	0.00
	0*	0.66
	1.4	0.36
	4.6	0.33
	10.3	0.23

Figure 1. a.) Schematic of a model membrane coated electrocatalyst (MCEC) comprised of a silicon oxide (SiO$_x$)-encapsulated Pt thin film for which a generic electrochemical reaction, O+n·e$^-$→R, is shown occurring at the buried interface between the SiO$_x$ and Pt. The catalytic Pt layer and Ti adhesion layer are supported on a flat, conductive support. Layer thicknesses are not drawn to scale. b.) AFM image of an as-synthesized 10.3 nm SiOx layer deposited on top of a 50/4.5 nm thick Pt/Ti thin film on a p$^+$Si substrate. The values in the scale-bar for the AFM image correspond to the deviation of the local z-height from the average z-height.
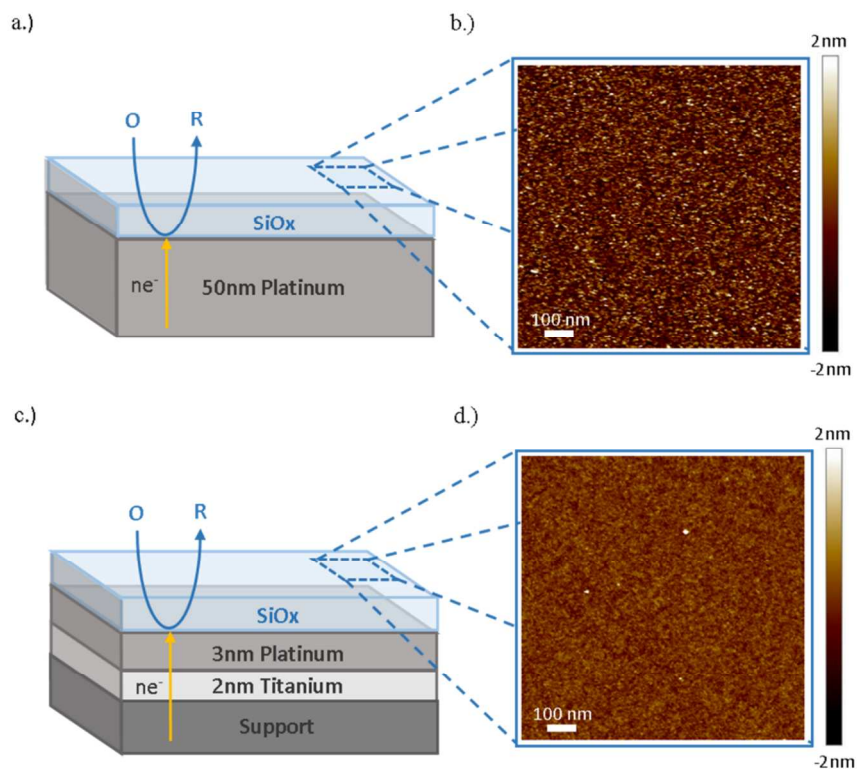
Figure 2. a.) XPS Pt 4f spectra of two unencapsulated Pt electrodes ("Bare Pt" and "UV ozone Pt") and a SiO$_x$|(thick Pt) electrode with t$_{SiOx}$=1.4 nm. The spectra were normalized to the maximum Pt 4f 7/2 peak intensities for all samples. b.) Pt 4f difference spectra (grey curves) obtained by subtracting the spectrum of the untreated bare Pt electrode from those of the PtO$_x$-containing electrodes. The black dashed lines represent the fitted background and overall fitted spectra.
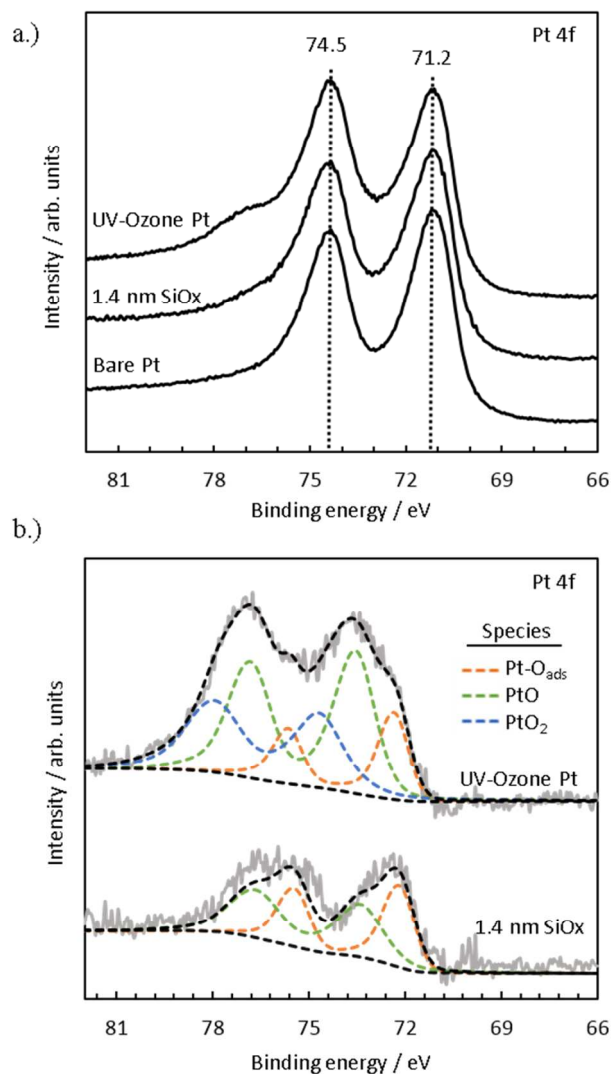
Figure 3. a.) First segment of the first CV scan for t_{SiOx}= 0, 1.4, 4.6, and 10.3 nm SiO_x|(thick Pt) electrodes. Steady state CV curves measured over b.) narrow and c.) wide potential windows for the same electrodes used in a.). All CVs were conducted at 100 mV s^{-1} in deaerated 0.5 M H_2SO_4.
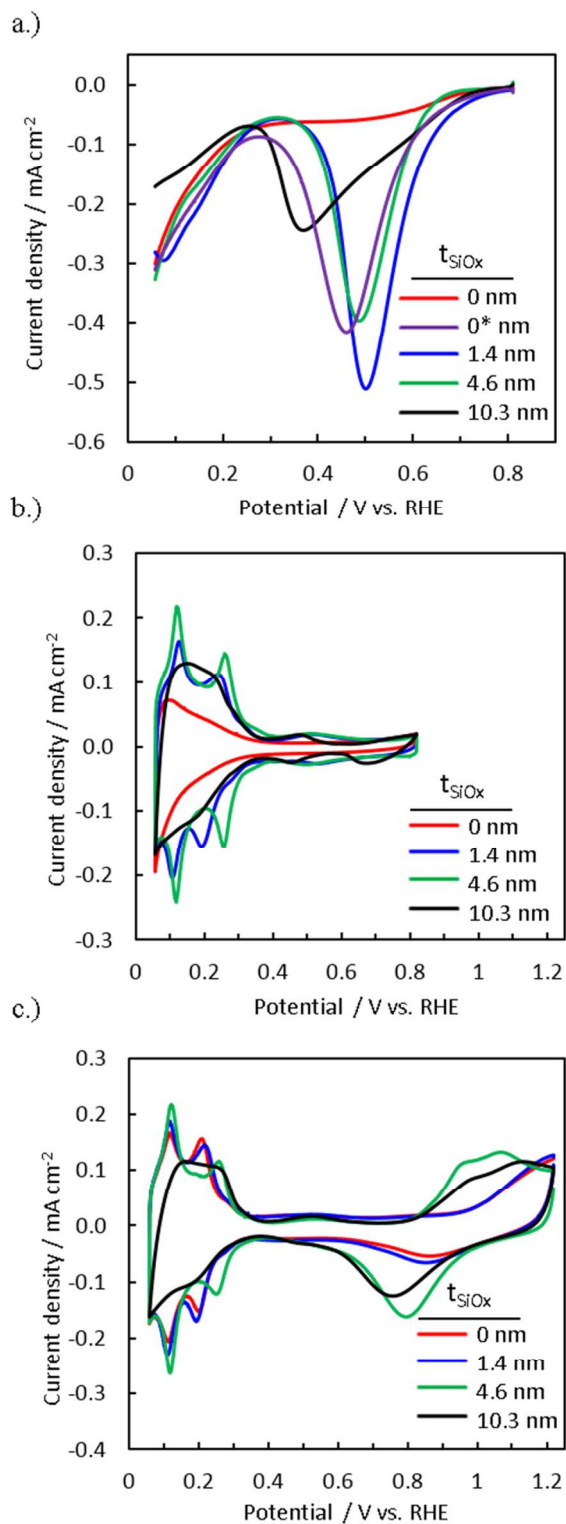
**Figure 4.** XPS analysis of bare Pt and SiO$_x$|Pt electrodes based on thin and thick Pt films. a.) Ti 2p spectra for bare Pt films before and after UV ozone treatment. b.) Pt 4f spectra for bare thick (50 nm) and thin (3 nm) Pt layers. In b.), the solid black curve is the raw spectra and the solid grey curve is the fitted background signal.
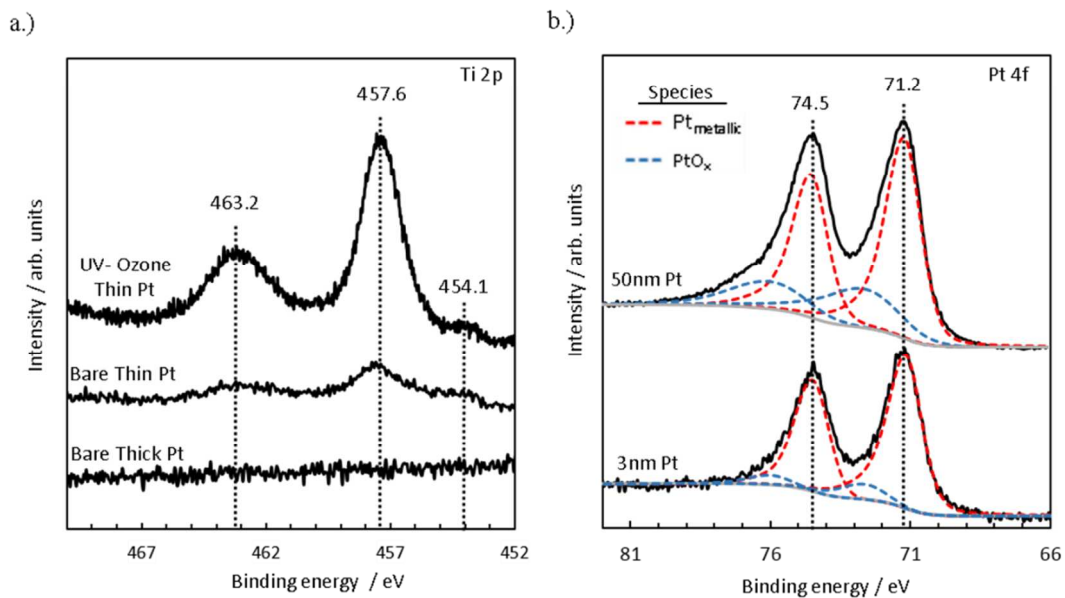
Figure 5. a.) First segment of the first CV scan for t_{SiOx}= 0, 1.6, 4.8, and 7.9 nm SiO_x|(thin Pt) electrodes based on a 3 nm thick Pt layer. Steady state CV curves measured over b.) narrow and c.) wide potential windows for the same electrodes used in a.). All CVs were conducted at 100 mV s^{-1} in deaerated 0.5 M H_2SO_4.

40
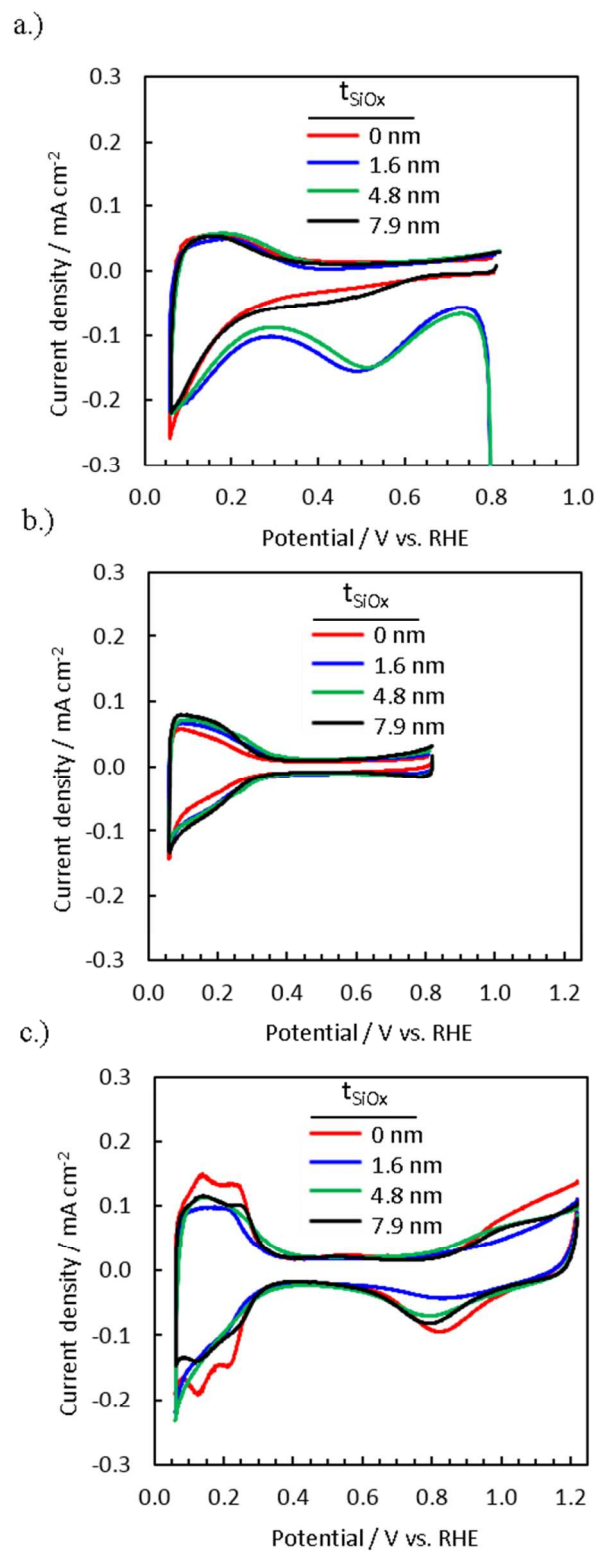
Figure 6. Cu stripping voltammetry difference curves for electrodes based on SiO_x overlayers deposited on a.) thin (3 nm) Pt substrates and b.) thick (50 nm) Pt substrates. The curves in a.) and b.) are given by the difference between LSV curves measured at 100 mV s^{-1} in 0.1 M H_2SO_4 (supporting electrolyte) and 2 mM $CuSO_4$ + 0.1 M H_2SO_4. c.) Comparison of the ECSA of the $SiO_x|Pt$ electrodes based on Cu_{upd} signal, shown as a function of SiO_x thickness (t_{SiOx}).
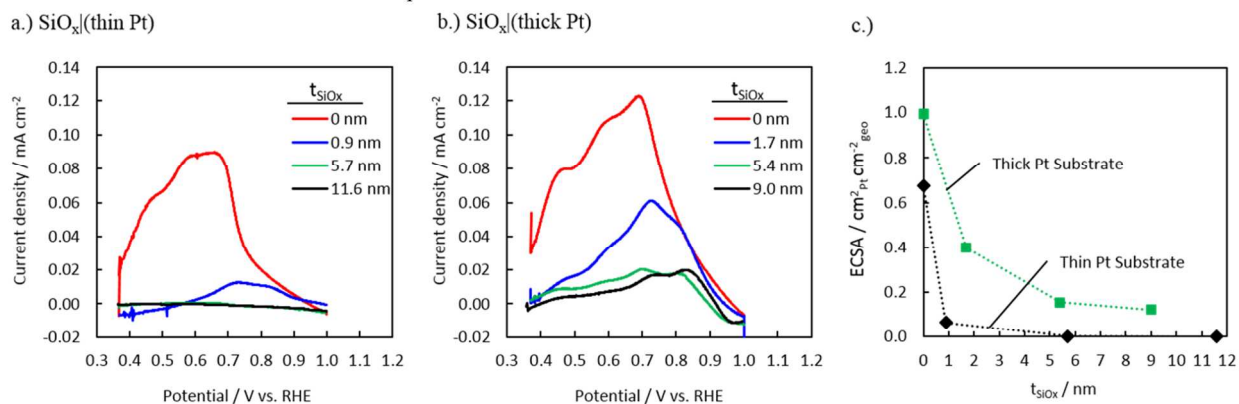
Figure 7. LSV curves in dearated 0.5 M H_2SO_4 for SiO_x|Pt electrodes based on a.) thin (3 nm) Pt substrates and b.) thick (50 nm) Pt substrates. LSV curves were carried out at 20 mV s^{-1} immediately after 1 hour of CV cycling in the same electrolyte between 0.06 and 0.82 V vs. RHE. No iR correction has been performed on this data. c.) A comparison of the overpotentials for the hydrogen evolution reaction (η_{HER}) at a current density of -20 mA cm^{-2} for all samples as a function of SiO_x thickness (t_{SiOx}).
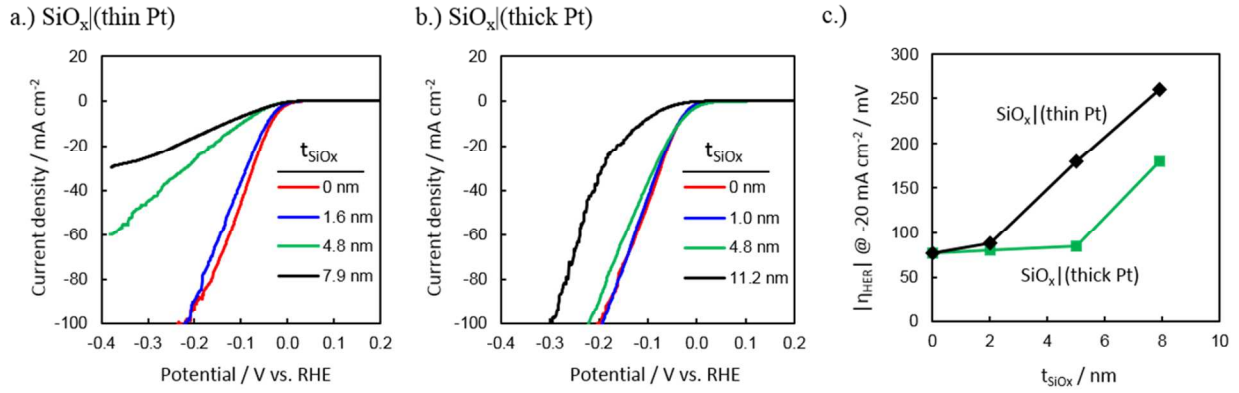
Figure 8. AFM images of SiO_x|Pt electrodes before and after 1 hour of CV cycling in deaerated 0.5 M H_2SO_4 over narrow (0.06 V-0.82 V vs. RHE) and wide (0.06 V-1.22 V vs. RHE) potential windows. Representative AFM images are shown for a.) SiO_x|(thin Pt) electrodes and b.) SiO_x|(thick Pt) electrodes with two different SiO_x thicknesses. c.) Rms roughness values, taken as the average value obtained from 3 different images for each sample.
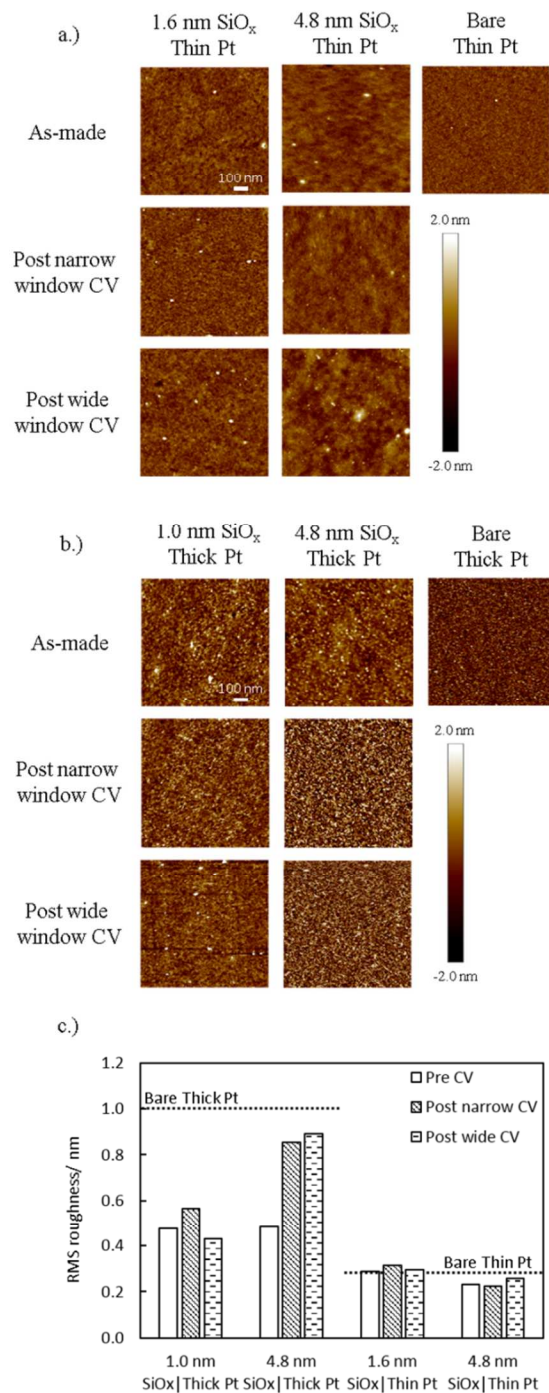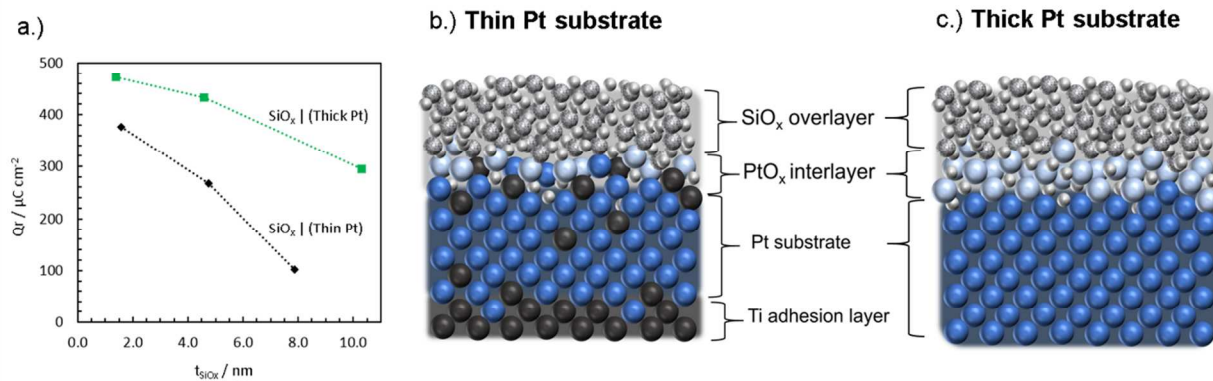
Figure 9. Schematic side-views of as-made $SiO_x|Pt$ electrodes made from depositing SiO_x on a.) a thick (bulk) Pt substrate and b.) a thin bilayer Pt/Ti substrate. In both schematics, the dark blue and light blue spheres represent Pt atoms in metallic (Pt^0) and oxidized (PtO_x) states, respectively.

This article identifies Pt-oxide interlayers at the buried interface of Si-oxide/Pt thin films and explores their implications for electrocatalysis.